Multispeed entropic lattice Boltzmann model for thermal flows

N. Frapolli,* S. S. Chikatamarla,† and I. V. Karlin‡
Department of Mechanical and Process Engineering, ETH Zurich, 8092 Zurich, Switzerland
(Received 25 July 2014; published 30 October 2014)

An energy-conserving lattice Boltzmann (LB) model based on the entropic theory of admissible higher-order lattice is presented in detail. The entropy supporting 'zero-one-three" lattice is used to construct a model capable of reproducing the full Fourier-Navier-Stokes equations at low Mach numbers. The proposed direct approach of constructing thermal models overcomes the shortcomings of existing models and retains one of the most important advantages of the LB methods, the exact space discretization of the advection step, thus paving the way for direct numerical simulation of thermal flows. New thermal wall boundary condition capable of handling curved geometries immersed in a multispeed lattice is proposed by extending the Tamm-Mott-Smith boundary condition. Entropic realization of the current model ensures stability of the model also for subgrid simulations. Numerical validation and thermodynamic consistency is demonstrated with classical setups such as thermal Couette flow, Rayleigh-Bénard natural convection, acoustic waves, speed of sound measurements, and shock tube simulations.

DOI: 10.1103/PhysRevE.90.043306 PACS number(s): 47.11.−j, 05.20.Dd

I. INTRODUCTION

The lattice Boltzmann method (LBM) has become, in recent years, a particularly attractive approach in the simulation of fluid dynamics problems, covering a broad range of applications: turbulent flows [1], microflows, porous media, multiphase flows [2], relativistic hydrodynamic, and beyond [3]. The LB method solves numerically a discrete set of kinetic equations for the populations $f_i(\boldsymbol{x},t)$, designed to reproduce, in the hydrodynamic limit, the desired set of equations; or in case of thermal and compressible flows, the thermohydrodynamic equations. Each population is associated with a discrete velocity $\boldsymbol{c}_i$ that fits into a regular spatial lattice with nodes $\boldsymbol{x}$ at time t. This formulation enables a simple and highly efficient "stream-along-links-and-equilibrate-at-nodes" realization of the LB method algorithm, which is key to both computational efficiency and numerical accuracy of the scheme.

Primary success of the LB method resides in the simulation of incompressible flows on standard lattices with relatively few velocities [4–7]; exceptional performance has been achieved recently with the unconditionally stable entropic lattice Boltzmann method (ELBM) [8], which enables simulation of turbulent incompressible flows at high Reynolds number and in complex geometries [9,10]. In spite of the relative success of the LBM as a tool for simulation of isothermal flows, a similar systematic extension to thermal and fully compressible flows still remains a challenge. In fact, conventional direct numerical simulation (DNS) solvers also face a number of difficulties in simulating compressible flows. The problems range from the need for highly nondissipative numerical methods to the abrupt increase of the computational costs, in particular with increasing Mach numbers [11]. Given the promising results obtained for the simulation of high Reynolds number turbulent flows in complex geometries with the ELBM, and the prohibitive computational costs of conventional compressible DNS solvers for practical computations, ELBM solvers for compressible flows would be a very welcome solution to the problem.

Despite a number of suggestions found in the literature, broadly three main approaches are followed by various authors. The first approach employs standard LB lattices to tackle compressible flows, due to the ease and simplicity of the lattice [12]. However, due to lack of sufficient isotropy on these standard lattices, one needs to introduce correction terms that require evaluation of gradients of velocity, temperate, stresses, etc., at each lattice site [13]. Such an approach of evaluating correction terms increases the complexity of the code in the presence of walls. Also, such an approach surrenders the main advantage of LB methods, namely locality of computations, which affects not just the computational efficiency and simplicity but also the accuracy of the method.

Alternatively, one can avoid introduction of correction terms on standard lattice by using two sets of partially or fully coupled populations instead of just one. The first lattice is used for mass and momentum computations (recovering continuity and momentum equations), as in the case of isothermal LBM, while the other lattice is used for the temperature dynamics [14]. However, this coupling in the formulation of Ref. [14] is nonlocal, increasing the complexity of the model. In particular, physical effects such as viscous heating do not emerge naturally and need to be introduced by forcing terms. More recently, total energy was chosen instead of the internal energy as the conserved quantity on the second lattice [15,16] to avoid nonlocality of computations. However, this approach still cannot be used for simulation of compressible flows at moderate Mach numbers or acoustics owing to the lack of sufficient isotropy of the first lattice.

Finally, the third approach avoids the introduction of correction terms and the use of a second set of populations by using lattices with more discrete velocities (multispeed lattices), required to adequately represent the moment system necessary to obtain the full thermal Fourier-Navier-Stokes equations. Early attempts such as Refs. [17,18], however,

*frapolli@lav.mavt.ethz.ch
†chikatamarla@lav.mavt.ethz.ch
‡karlin@lav.mavt.ethz.ch

 ©2014 American Physical Society

could not be successfully employed as the corresponding LB models were numerically unstable. Nevertheless, with the recent progresses in the theory of admissible higher-order lattices [19–25], a systematic development of thermal and compressible LB models has become possible. Although, the employment of higher-order lattices has been limited so far due to the complexity of such models, in particular for what concerns wall boundary conditions. Moreover, some multispeed models expect to use noninteger valued lattice speeds [26–29], thus subjecting the models to the deficiencies arising from nonlocal computations (need of higher-order nondissipative numerical interpolation schemes and complexities near curved wall boundaries).

In this paper, theory of admissible higher-order lattices is briefly reviewed, based on the previous work of Refs. [19,20], and the resulting regular space-filling zero-one-three (ZOT) lattice is then used. In particular, two-dimensional realization of ZOT lattice, the D2Q25, is employed to construct an entropic thermal and compressible LB model. The increased accuracy and isotropy of the lattice allows us to obtain a moment system, which guarantees the correct recovery of the Fourier-Navier-Stokes equations in the hydrodynamic limit, for moderate Mach number flows, with sufficiently high accuracy. Moreover, extension to the entropic lattice Boltzmann formulation is presented in detail, and is generalized for variable Prandlt number flows using the quasiequilibrium realization.

The outline of the paper is as follows: in Sec. II we present in detail the higher-order entropic thermal lattice Boltzmann method for weakly compressible flows together with the derivation of the lattice and corresponding equilibria. In Sec. II B we expose the quasiequilibrium method described in Ref. [30], which allows variable Prandtl numbers. In Secs. II C and II D the Chapman-Enskog method is used to derive the thermohydrodynamic limit for the BGK and of the quasiequilibrium realizations of this model. Section II F contains a detailed presentation of a new TMS wall boundary condition needed for multispeed lattices. The differences with similar types of boundary conditions for higher-order lattices [31] are also discussed in detail. The theoretical part of the paper concludes with the entropic thermal lattice Boltzmann formulation for high Reynolds (and Rayleigh) number simulations, in Sec. II G. In Sec. III, the numerical validation of the model is performed by means of five standard two-dimensional setups: the thermal Couette flow, the Rayleigh-Bénard natural convection, the linear and nonlinear sound waves, the speed of sound measurements, and the shock tube problem. In Sec. IV we will draw the conclusions.

II. HIGHER-ORDER THERMAL LATTICE BOLTZMANN MODEL

The first step toward the derivation of a thermodynamically consistent higher-order thermal lattice Boltzmann model is to find a lattice with more velocities and isotropy with respect to standard lattices. In the next section, the methodology employed for the derivation of such admissible lattices is briefly presented, together with the natural extension of the standard lattice D2Q9 to the ZOT lattice D2Q25.

A. Admissible higher-order lattices

One way of deriving admissible higher-order lattices has been presented by Refs. [32,33] and involves discretizing the Boltzmann equation on the roots of Hermite polynomials. Although this method provides a systematic derivation of new complete Galilean-invariant models, since the roots of the Hermite polynomials are irrational, the corresponding discrete velocities cannot be incorporated into a regular space-filling lattice, thereby losing one of the most important advantages of the LBM: the exact space discretization of the advection step. Alternatively, presented in Refs. [19,20] is a different systematic approach, based on the minimization of a discrete entropy function H given the weights W_i,

$$H = \sum_{i=1}^{Q} f_i \ln\left(\frac{f_i}{W_i}\right), \tag{1}$$

which provides integer-valued discrete-velocity models, or, in the limiting case, the Gauss-Hermite-based models. One of the most important results obtained by this derivation is the natural extension of the D2Q9 model, with base velocities $\boldsymbol{c}_i = \{0, \pm 1\}$, to the D2Q25 model, with base velocities $\boldsymbol{c}_i = \{0, \pm 1, \pm 3\}$ (in two dimensions).

The derivation of the D2Q25-ZOT model is based on the construction of the one-dimensional D1Q5-ZOT model and it consists in minimizing the entropy function H under the constraints of mass ρ, momentum ρu, and pressure tensor P^{eq} (or total energy in 1D),

$$\rho = \sum_{i=1}^{Q} f_i^{\mathrm{eq}}, \quad \rho u = \sum_{i=1}^{Q} f_i^{\mathrm{eq}} c_i,$$
$$P^{\mathrm{eq}} = \sum_{i=1}^{Q} f_i^{\mathrm{eq}} c_i^2 = \rho T + \rho u^2,$$

by expanding f_i^{eq} in power series of velocity u, in order to recover the weights W_i associated to the prescribed set of velocities $\boldsymbol{c}_i$. For the ZOT model, this amounts to finding the weights W_0, $W_{\pm 1}$, and $W_{\pm 3}$. Two- and three-dimensional extensions are obtained by taking tensor product of two or three one-dimensional discrete velocities, respectively, and by algebraic product of the corresponding one-dimensional weights. In two-dimensions, the weights read

$$\begin{aligned}
W_{(0,0)} &= \frac{1}{81}[T(3T-10)+9]^2,\\
W_{(0,\pm 1)} &= \frac{T}{48}(3-T)[T(3T-10)+9],\\
W_{(\pm 1,\pm 1)} &= \frac{9T^2}{256}(T-3)^2,\\
W_{(0,\pm 3)} &= \frac{T}{1296}(3T-1)[9+T(3T-10)],\\
W_{(\pm 1,\pm 3)} &= \frac{T^2}{768}(T-3)(1-3T),\\
W_{(\pm 3,\pm 3)} &= \frac{T^2}{20\,736}(1-3T)^2.
\end{aligned} \tag{2}$$

It is evident, that all the weights except $W_{(0,0)}$ have a singularity for the temperature at $T = 1/3$ or $T = 3$. This means that the range of temperature supported by the present lattice is confined between $1/3$ and 3 to guarantee positivity of the equilibrium populations. It must be mentioned that these new temperature-dependent weights are important for finding the equilibrium populations in the entropic lattice Boltzmann scheme. Constant values for the weight functions do not lead to an analytical expression for the equilibrium populations (desirable for computational efficiency), since one needs to solve then four coupled polynomial equations of order nine (in Lagrange multipliers). This has so far precluded efficient ELBM schemes for thermal flows. We now solve the problem by introducing temperature dependent weights in the entropy function Eq. (1). Once the weights are known, equilibrium populations are recovered by minimization of the entropy function H Eq. (1) with given weights Eq. (2), and under constraints of local conservation:

$$\begin{aligned} \rho &= \sum_{i=1}^{Q} f_i^{\mathrm{eq}}, \quad \rho u_\alpha = \sum_{i=1}^{Q} f_i^{\mathrm{eq}} c_{i\alpha}, \\ 2\rho E &= \sum_{i=1}^{Q} f_i^{\mathrm{eq}} c_{i\alpha} c_{i\alpha} = D\rho T + \rho u_\alpha u_\alpha, \end{aligned} \tag{3}$$

where $2\rho E$ is the total energy.

The minimization problem to find the equilibrium can be written using the method of Lagrange multipliers as

$$\begin{aligned} &\frac{dH}{df_i} + \chi' \frac{d}{df_i} f_i + \zeta_x' \frac{d}{df_i} c_{ix} f_i \\ &\quad + \zeta_y' \frac{d}{df_i} c_{iy} f_i + \gamma' \frac{d}{df_i} c_i^2 f_i = 0, \end{aligned} \tag{4}$$

where χ', ζ_x', ζ_y', and γ' are Lagrange multipliers corresponding to the conservation of mass, x momentum, y momentum, and total energy, respectively. The equilibrium populations can now be computed in the product form as

$$f_i^{\mathrm{eq}} = \rho\, W_i\, \chi\, \zeta_x^{c_{ix}}\, \zeta_y^{c_{iy}}\, \gamma^{c_{i\alpha} c_{i\alpha}}. \tag{5}$$

Power series expansions of Lagrange multipliers are performed to eight-order in u and are presented in the Appendix. This product form of evaluation of equilibrium, although restricted to small values of velocity u, is extremely efficient for multispeed lattices [34]. In two dimensions, one writes just four polynomial expressions (for Lagrange multipliers) instead of 25 polynomial expressions, one for each discrete velocity. One could alternatively also use the regular series expansion of local Maxwellian as the equilibrium populations; since the product when expanded and truncated to the same order recover the very same expressions. However, one *must* truncate the expansion of local Maxwellian to relevant orders of u (in the present case of D2Q25 u^3) to ensure the equilibrium populations are consistent with the isotropy of the lattice and to ensure local conservation laws.

Once the local equilibrium is computed by minimizing the entropy, we can verify the isotropy of the lattice and the equilibrium distributions by looking at the moments implied by the equilibrium. As described by Ref. [20], the ZOT lattice and the associated entropic equilibrium recovers the third-order moment $Q_{\alpha\beta\gamma}^{\mathrm{eq}}$ of the Maxwellian and the fourth order moment $R_{\alpha\beta\gamma\mu}^{\mathrm{eq}}$ until fourth order in velocity; the set of moments can be written then:

$$\begin{aligned} Q_{\alpha\beta\gamma}^{\mathrm{eq}} &= \sum_{i=1}^{Q} f_i^{\mathrm{eq}} c_{i\alpha} c_{i\beta} c_{i\gamma} = \rho T(u_\alpha \delta_{\beta\gamma} + u_\beta \delta_{\alpha\gamma} + u_\gamma \delta_{\alpha\beta}) \\ &\quad + \rho u_\alpha u_\beta u_\gamma + \mathcal{O}(u^5, u^3 \Delta T, u \Delta T^2), \end{aligned} \tag{6}$$

$$\begin{aligned} R_{\alpha\beta}^{\mathrm{eq}} &= \sum_{i=1}^{Q} f_i^{\mathrm{eq}} c_{i\alpha} c_{i\beta} c_i^2 = \rho T[(D+2)T + u^2]\delta_{\alpha\beta} \\ &\quad + \rho u_\alpha u_\beta (D+4)T + \mathcal{O}(u^4, u^2 \Delta T, \Delta T^2), \end{aligned} \tag{7}$$

where $R_{\alpha\beta}^{\mathrm{eq}}$ is the contracted fourth-order moment and D is the spatial dimension. It will be clear in the following section the role played by these two higher-order moments in recovering the thermohydrodynamic limit. The terms recovered here are the minimal required for correctly deriving energy equation in the hydrodynamic limit.

B. Lattice Boltzmann equation: Standard BGK and quasiequilibrium models

The simplest way to set up a lattice Boltzmann kinetic equation is to employ the single relaxation time Bhatnagar-Gross-Krook (LBGK) model,

$$f_i(\boldsymbol{x} + \boldsymbol{c}_i \delta t, t + \delta t) - f_i(\boldsymbol{x}, t) = \omega \left(f_i^{\mathrm{eq}} - f_i \right), \tag{8}$$

where ω is the relaxation parameter related to viscosity and thermal conductivity, $\delta t = 1$ is the time step, and f_i^{eq} is the local equilibrium Eq. (5) that satisfies local conservation laws Eq. (3). Since viscosity and thermal diffusivity are related to the same parameter ω, the BGK model implies a fixed Prandtl number ($\mathrm{Pr} = \mathrm{Pr}_{\mathrm{BGK}} = 1$). This restriction can be overcome by introducing an intermediate relaxation state in the BGK models, namely the quasiequilibrium state. The relaxation process can now be seen as a two-step process in which the population relaxes toward a quasiequilibrium state and the quasiequilibrium itself relaxes toward local equilibrium. The kinetic equation reads as

$$\begin{aligned} &f_i(\boldsymbol{x} + \boldsymbol{c}_i \delta t, t + \delta t) - f_i(\boldsymbol{x}, t) \\ &\quad = \omega_1 (f_i^* - f_i) + \omega_2 \left(f_i^{\mathrm{eq}} - f_i^* \right), \end{aligned} \tag{9}$$

where ω_1 and ω_2 are the two relaxation parameters related to viscosity and thermal conductivity, which will be specified in the next section, and f_i^* represents the quasiequilibrium state, which in addition to the conserved quantities, is designed to conserve also the prescribed "slow variables" or "quasiconserved quantities." Following Ref. [30], the quasiequilibrium populations f_i^* here are required to satisfy the conservation of mass, momentum, and total energy,

$$\begin{aligned} \rho &= \sum_{i=1}^{Q} f_i^*, \quad \rho u_\alpha = \sum_{i=1}^{Q} f_i^* c_{i\alpha}, \\ 2\rho E &= D\rho T + \rho u_\alpha u_\alpha = \sum_{i=1}^{Q} f_i^* c_{i\alpha} c_{i\alpha}, \end{aligned} \tag{10}$$

and additionally, if $\mathrm{Pr} < \mathrm{Pr}_{\mathrm{BGK}}$, the centered heat flux tensor

$$\underline{Q}_{\alpha\beta\gamma} = \sum_{i=1}^{Q} f_i^*(c_{i\alpha} - u_\alpha)(c_{i\beta} - u_\beta)(c_{i\gamma} - u_\gamma), \tag{11}$$

is conserved; and if $\mathrm{Pr} > \mathrm{Pr}_{\mathrm{BGK}}$, the centered stress tensor

$$\underline{P}_{\alpha\beta} = \sum_{i=1}^{Q} f_i^*\left[(c_{i\alpha} - u_\alpha)(c_{i\beta} - u_\beta) - \frac{2}{D}\delta_{\alpha\beta}(\boldsymbol{c}_i - \boldsymbol{u}_i)^2\right], \tag{12}$$

needs to be conserved. Such a distinction between the cases of Prandtl number higher or lower than $\mathrm{Pr}_{\mathrm{BGK}}$ is necessary to ensure compliance with the entropy principle (see Ref. [30] for more details).

C. Hydrodynamic limit of the ZOT LB model with BGK collision

Let us first derive the hydrodynamic limit of the multispeed lattice, for BGK collision model, and then for the case of the quasiequilibrium model. Since the quasiequilibrium model described by Eq. (9) reduces to the BGK model Eq. (8) for $\omega_1 = \omega_2 = \omega$, we proceed by with the general case and specify the differences between the BGK and quasiequilibrium models as we proceed. The thermohydrodynamic limit of the kinetic Eq. (9) is derived using the Chapman-Enskog method, under the assumption the moments Eqs. (6) and (7) are satisfied by the equilibrium populations. We start by expanding the shift operator in a Taylor series until second order,

$$\left[\delta t(\partial_t + \partial_\mu c_{i\mu}) + \frac{\delta t^2}{2}(\partial_t + \partial_\mu c_{i\mu})(\partial_t + \partial_\nu c_{i\nu})\right] f_i = \omega_1(f_i^* - f_i) + \omega_2\left(f_i^{\mathrm{eq}} - f_i^*\right), \tag{13}$$

and by introducing a characteristic time scale of the flows, Θ, and a reduced time $t' = t/\Theta$. Similarly, we introduce reduced velocities and reduced coordinate, $c_i' = c_i/c$ and $x' = x/(c\Theta)$, where $c = 1$, and we rewrite Eq. (13) in terms of the reduced variables t', x', and drop primes for simplicity of notation. After introduction of the smallness parameter $\epsilon = \delta t/\Theta$, Eq. (13) can be written as

$$\left[\epsilon(\partial_t + \partial_\mu c_{i\mu}) + \frac{\epsilon^2}{2}(\partial_t + \partial_\mu c_{i\mu})(\partial_t + \partial_\nu c_{i\nu})\right] f_i = \omega_1(f_i^* - f_i) + \omega_2\left(f_i^{\mathrm{eq}} - f_i^*\right). \tag{14}$$

We can now perform a multiscale expansion of the time derivative operator, the populations and quasiequilibrium populations to second order as

$$\epsilon\partial_t = \epsilon\partial_t^{(1)} + \epsilon^2\partial_t^{(2)} + \cdots \tag{15}$$

$$f_i = f_i^{(0)} + \epsilon f_i^{(1)} + \epsilon^2 f_i^{(2)} + \cdots \tag{16}$$

$$f_i^* = f_i^{*(0)} + \epsilon f_i^{*(1)} + \epsilon^2 f_i^{*(2)} + \cdots \tag{17}$$

After introduction of Eqs. (15)–(17) in Eq. (14), analysis to order $\epsilon^{(0)}$, $\epsilon^{(1)}$, and $\epsilon^{(2)}$ is performed, and $\mathrm{Pr}_{\mathrm{BGK}}$ is identified.

Terms to the order $\epsilon^{(0)}$ lead to

$$f_i^{(0)} = f_i^{*(0)} + \frac{\omega_2}{\omega_1}\left(f_i^{\mathrm{eq}} - f_i^{*(0)}\right); \tag{18}$$

since $f_i^{*(0)}$ is designed to ensure $f_i^{*(0)} = f_i^{\mathrm{eq}}$, we find that the leading term in the expansion Eq. (16) is the local equilibrium,

$$f_i^{(0)} = f_i^{\mathrm{eq}}. \tag{19}$$

Local conservation laws imply

$$\sum_{i=0}^{Q}\left\{1, c_{i\alpha}, c_i^2\right\} f_i = \sum_{i=0}^{Q}\left\{1, c_{i\alpha}, c_i^2\right\} f_i^{\mathrm{eq}}, \tag{20}$$

which combined with Eqs. (16) and (19) lead to the solvability conditions

$$\sum_{i=0}^{Q}\left\{1, c_{i\alpha}, c_i^2\right\} f_i^{(1)} = \sum_{i=0}^{Q}\left\{1, c_{i\alpha}, c_i^2\right\} f_i^{(2)} = \cdots = 0. \tag{21}$$

Collecting terms to the order $\epsilon^{(1)}$, we obtain an expression for the first-order population,

$$f_i^{(1)} = f_i^{*(1)}\left(1 - \frac{\omega_2}{\omega_1}\right) - \frac{1}{\omega_1}\left(\partial_t^{(1)} + \partial_\mu c_{i\mu}\right) f_i^{(0)}. \tag{22}$$

Applying solvability conditions Eq. (21) to Eq. (22), and using the conditions

$$\sum_{i=0}^{Q}\left\{1, c_{i\alpha}, c_i^2\right\} f_i^{*(1)} = 0, \tag{23}$$

for the quasiequilibrium populations, the thermohydrodynamic equations of mass, momentum, and energy are recovered to first order:

$$\partial_t^{(1)}\rho = -\partial_\alpha(\rho u_\alpha), \tag{24}$$

$$\partial_t^{(1)} u_\alpha = -u_\beta\partial_\beta u_\alpha - \frac{1}{\rho}\partial_\alpha(\rho T), \tag{25}$$

$$\partial_t^{(1)} T = -u_\alpha\partial_\alpha T - \frac{2}{D}T(\partial_\alpha u_\alpha), \tag{26}$$

where the term ρT can be identified as $p = \rho T$, which is equation of state for ideal gases, with p being the pressure.

For the simple BGK model, we have that $\omega_1 = \omega_2 = \omega$, and collecting terms to order $\epsilon^{(2)}$ in Eq. (14) we obtain

$$\left[\partial_t^{(2)} - \left(\frac{1}{\omega} - \frac{1}{2}\right)\left(\partial_t^{(1)}\partial_t^{(1)} + \partial_\mu\partial_\nu c_{i\mu}c_{i\nu} + 2\partial_t^{(1)}\partial_\mu c_{i\mu}\right)\right] f_i^{(0)} = -\omega f_i^{(2)}. \tag{27}$$

Applying solvability conditions Eq. (21) to Eq. (27), and making use of Eqs. (24) and (25), we find, for the mass,

$$\partial_t^{(2)}\rho = 0, \tag{28}$$

meaning second-order contribution to continuity equation vanishes. Second-order terms in the momentum equation reads

$$\partial_t^{(2)}(\rho u_\alpha) = \left(\frac{1}{\omega} - \frac{1}{2}\right)\partial_\beta\left(\partial_t^{(1)} P_{\alpha\beta}^{\mathrm{eq}} + \partial_\gamma Q_{\alpha\beta\gamma}^{\mathrm{eq}}\right). \tag{29}$$

By computing first-order derivative of $P^{\rm eq}_{\alpha\beta}$, spatial derivative of $Q^{\rm eq}_{\alpha\beta\gamma}$, using chain rule and combining with the results Eqs. (24)–(26), we find

$$\partial_t^{(2)} u_\alpha = -\frac{1}{\rho}\partial_\beta \Pi_{\alpha\beta}, \tag{30}$$

where $\Pi_{\alpha\beta}$ is the nonequilibrium pressure tensor,

$$\Pi_{\alpha\beta} = -\mu\left(S_{\alpha\beta} - \frac{2}{D}\partial_\gamma u_\gamma \delta_{\alpha\beta}\right), \tag{31}$$

with the strain rate tensor $S_{\alpha\beta}$ defined, for the BGK model, as

$$S_{\alpha\beta} = \partial_\alpha u_\beta + \partial_\beta u_\alpha, \tag{32}$$

and

$$\mu = \left(\frac{1}{\omega} - \frac{1}{2}\right)\rho T, \tag{33}$$

the viscosity of the BGK model. Solvability condition Eq. (21) to Eq. (27) for the second-order terms in the energy equation imply

$$\partial_t^{(2)}(2\rho E) = \left(\frac{1}{\omega} - \frac{1}{2}\right)\partial_\alpha\left(\partial_t^{(1)} q^{\rm eq}_\alpha + \partial_\beta R^{\rm eq}_{\alpha\beta}\right). \tag{34}$$

The left-hand side of Eq. (34) is transformed using second-order time derivatives of mass and momentum, Eqs. (28) and (30):

$$\partial_t^{(2)}(2\rho E) = D\rho\partial_t^{(2)} T - 2u_\alpha \partial_\beta \Pi_{\alpha\beta}. \tag{35}$$

The right-hand side of Eq. (34) is transformed by computing explicitly first-order time derivative of $q^{\rm eq}_\alpha$ and spatial derivative of $R^{\rm eq}_{\alpha\beta}$, and by making use of and Eqs. (24)–(26). After some algebra and neglecting fourth-order terms in velocity, as pertinent for the low Mach number assumption, we obtain

$$\begin{aligned}\partial_t^{(1)} q^{\rm eq}_\alpha + \partial_\beta R^{\rm eq}_{\alpha\beta} = {} & 2\rho T u_\beta\left[S_{\alpha\beta} - \frac{2}{D}(\partial_\gamma u_\gamma)\delta_{\alpha\beta}\right] \\ & +(D+2)\rho T\partial_\alpha T.\end{aligned} \tag{36}$$

By substitution of Eqs. (35) and (36) in Eq. (34), we obtain the second-order derivative of the temperature:

$$\partial_t^{(2)} T = \frac{2}{\rho D}\partial_\alpha(\kappa\partial_\alpha T) - \frac{2}{\rho D}(\partial_\alpha u_\beta)\Pi_{\alpha\beta}, \tag{37}$$

where κ is the thermal conductivity of the BGK model given by

$$\kappa = \frac{D+2}{2}\left(\frac{1}{\omega} - \frac{1}{2}\right)\rho T. \tag{38}$$

Summing up the contribution of first and second order, the final temperature equation reads

$$\begin{aligned}\partial_t T = {} & -u_\alpha\partial_\alpha T - \frac{2}{D}T(\partial_\alpha u_\alpha) \\ & -\frac{2}{\rho D}(\partial_\alpha u_\beta)\Pi_{\alpha\beta} + \frac{2}{\rho D}\partial_\alpha(\kappa\partial_\alpha T),\end{aligned} \tag{39}$$

with fixed Prandtl number $\mathrm{Pr}_{\rm BGK}$:

$$\mathrm{Pr}_{\rm BGK} = \frac{c_p\mu}{\kappa} = \frac{\frac{(D+2)}{2}\cdot\left(\frac{1}{\omega} - \frac{1}{2}\right)\rho T}{\frac{(D+2)}{2}\left(\frac{1}{\omega} - \frac{1}{2}\right)\rho T} = 1. \tag{40}$$

D. Hydrodynamic limit of the higher-order LB model with variable Prandtl number

When we consider the quasiequilibrium model for achieving variable Prandtl number, Eq. (27) has additional terms including the second-order quasiequilibrium population:

$$\begin{aligned}&\left[\partial_t^{(2)} + \tfrac{1}{2}\left(\partial_t^{(1)}\partial_t^{(1)} + \partial_\mu\partial_\nu c_{i\mu}c_{i\nu} + 2\partial_t^{(1)}\partial_\mu c_{i\mu}\right)\right] f_i^{(0)} \\ &\quad = \omega_1\left(f_i^{*(2)} - f_i^{(2)}\right) - \omega_2 f_i^{*(2)} - \left(\partial_t^{(1)} + \partial_\mu c_{i\mu}\right) f_i^{(1)}.\end{aligned} \tag{41}$$

Applying Eq. (22) for the first-order populations and considering that $f_i^{*(2)} = 0$, by construction, Eq. (41) becomes

$$\begin{aligned}&\left[\partial_t^{(2)} - \left(\frac{1}{\omega_1} - \frac{1}{2}\right)\left(\partial_t^{(1)}\partial_t^{(1)} + \partial_\mu\partial_\nu c_{i\mu}c_{i\nu} + 2\partial_t^{(1)}\partial_\mu c_{i\mu}\right)\right] f_i^{(0)} \\ &\quad = -\omega_1 f_i^{(2)} - \left(\partial_t^{(1)} + \partial_\mu c_{i\mu}\right) f_i^{*(1)}\left(1 - \frac{\omega_2}{\omega_1}\right).\end{aligned} \tag{42}$$

Applying solvability condition for mass, we obtain the same result as for the BGK model, Eq. (28),

$$\partial_t^{(2)}\rho = 0, \tag{43}$$

i.e., second-order contribution to the continuity equation vanishes. Solvability condition for momentum and energy equation recover

$$\begin{aligned}\partial_t^{(2)}(\rho u_\alpha) = {} & \left(\frac{1}{\omega_1} - \frac{1}{2}\right)\partial_\beta\left(\partial_t^{(1)} P^{\rm eq}_{\alpha\beta} + \partial_\gamma Q^{\rm eq}_{\alpha\beta\gamma}\right) \\ & -\left(1 - \frac{\omega_2}{\omega_1}\right)\partial_\beta P^{*(1)}_{\alpha\beta},\end{aligned} \tag{44}$$

$$\begin{aligned}\partial_t^{(2)}(2\rho E) = {} & \left(\frac{1}{\omega_1} - \frac{1}{2}\right)\partial_\alpha\left(\partial_t^{(1)} q^{\rm eq}_\alpha + \partial_\beta R^{\rm eq}_{\alpha\beta}\right) \\ & -\left(1 - \frac{\omega_2}{\omega_1}\right)\partial_\alpha q^{*(1)}_\alpha.\end{aligned} \tag{45}$$

From here on, a clear distinction between two cases, $\mathrm{Pr} < \mathrm{Pr}_{\rm BGK}$ and $\mathrm{Pr} > \mathrm{Pr}_{\rm BGK}$, has to be made, since the quasiequilibrium state, driven by the "slow variable" differs in the two cases. We start from the case where $\mathrm{Pr} < \mathrm{Pr}_{\rm BGK}$ deriving the appropriate expression for viscosity and thermal conductivity, and then we proceed similarly with the case $\mathrm{Pr} > \mathrm{Pr}_{\rm BGK}$.

1. $\mathrm{Pr} < \mathrm{Pr}_{\rm BGK}$

As previously introduced in Sec. II B, in the case $\mathrm{Pr} < \mathrm{Pr}_{\rm BGK}$, the additional quasiconserved quantity by the quasiequilibrium population is the centered heat transfer tensor, $\underline{Q}_{\alpha\beta\gamma}$, i.e.,

$$f^* = f^*(\rho, u_\alpha, 2\rho E, \underline{Q}_{\alpha\beta\gamma}). \tag{46}$$

The additional conserved term introduces additional constraints on the quasiequilibrium populations, and hence lead to the following first-order heat flux and first-order pressure tensor:

$$q^{*(1)}_\alpha = q^{(1)}_\alpha - 2u_\gamma P^{(1)}_{\alpha\gamma}, \tag{47}$$

$$P^{*(1)}_{\alpha\beta} = 0. \tag{48}$$

From Eq. (22) it is possible to obtain $q_\alpha^{(1)}$ as

$$q_\alpha^{(1)} = q_\alpha^{*(1)}\left(1-\frac{\omega_2}{\omega_1}\right) - \frac{1}{\omega_1}\left(\partial_t^{(1)} q_\alpha^{\rm eq} + \partial_\beta R_{\alpha\beta}^{\rm eq}\right), \tag{49}$$

and, by using Eq. (48), the first-order pressure tensor $P_{\alpha\beta}^{(1)}$,

$$P_{\alpha\beta}^{(1)} = -\frac{1}{\omega_1}\left(\partial_t^{(1)} P_{\alpha\beta}^{\rm eq} + \partial_\gamma Q_{\alpha\beta\gamma}^{\rm eq}\right). \tag{50}$$

By inserting Eq. (50) in Eq. (47) and Eq. (47) in Eq. (49), we obtain an expression for $q_\alpha^{*(1)}$:

$$q_\alpha^{*(1)} = -\frac{1}{\omega_2}\left(\partial_t^{(1)} q_\alpha^{\rm eq} + \partial_\beta R_{\alpha\beta}^{\rm eq}\right) - \frac{2u_\beta}{\omega_2}\left(\partial_t^{(1)} P_{\alpha\beta}^{\rm eq} + \partial_\gamma Q_{\alpha\beta\gamma}^{\rm eq}\right), \tag{51}$$

and computing explicitly the right-hand side of Eq. (51), we obtain

$$q_\alpha^{*(1)} = -\frac{1}{\omega_2}(D+2)\,\rho T\,\partial_\alpha T. \tag{52}$$

At this point, computation of second-order time derivative of momentum and energy is straight forward and is similar to the BGK model; using Eq. (48) we obtain the second-order momentum equation,

$$\partial_t^{(2)} u_\alpha = -\frac{1}{\rho}\partial_\beta \Pi_{\alpha\beta}, \tag{53}$$

where $\Pi_{\alpha\beta}$ is the nonequilibrium pressure tensor,

$$\Pi_{\alpha\beta} = -\mu\left(S_{\alpha\beta} - \frac{2}{D}\partial_\gamma u_\gamma \delta_{\alpha\beta}\right), \tag{54}$$

with

$$S_{\alpha\beta} = \partial_\alpha u_\beta + \partial_\beta u_\alpha, \tag{55}$$

the strain rate tensor, and

$$\mu = \left(\frac{1}{\omega_1} - \frac{1}{2}\right)\rho T, \tag{56}$$

the viscosity. The left-hand side of Eq. (45) is transformed using second-order time derivatives of mass and momentum, Eqs. (43) and (53):

$$\partial_t^{(2)}(2\rho E) = D\rho\partial_t^{(2)} T - 2u_\alpha \partial_\beta \Pi_{\alpha\beta}. \tag{57}$$

The right-hand side of Eq. (45) is transformed by computing explicitly first-order time derivative of $q_\alpha^{\rm eq}$ and spatial derivative of $R_{\alpha\beta}^{\rm eq}$, and by making use of Eqs. (24)–(26), and (52), we obtain

$$\partial_t^{(1)} q_\alpha^{\rm eq} + \partial_\beta R_{\alpha\beta}^{\rm eq} = (D+2)\rho T\partial_\alpha T + 2\rho T u_\beta\left[S_{\alpha\beta} - \frac{2}{D}(\partial_\gamma u_\gamma)\delta_{\alpha\beta}\right]. \tag{58}$$

By substitution of Eqs. (57) and (58) in Eq. (45), we obtain the second-order derivative of the temperature:

$$\partial_t^{(2)} T = \frac{1}{\rho D}\partial_\alpha(\kappa\partial_\alpha T) - \frac{2}{\rho D}(\partial_\alpha u_\beta)\Pi_{\alpha\beta}, \tag{59}$$

where κ is the thermal conductivity given by

$$\kappa = \frac{D+2}{2}\left(\frac{1}{\omega_2} - \frac{1}{2}\right)\rho T. \tag{60}$$

2. Pr > $\mathrm{Pr_{BGK}}$

When $\mathrm{Pr} > \mathrm{Pr_{BGK}}$, the additional quasiconserved variable is the traceless centered pressure tensor, i.e.,

$$f^* = f^*(\rho, u_\alpha, 2\rho E, \underline{\Theta}_{\alpha\beta}), \tag{61}$$

which imply the conditions

$$P_{\alpha\beta}^{*(1)} = P_{\alpha\beta}^{(1)}, \tag{62}$$

$$q_\alpha^{*(1)} = 2u_\gamma P_{\alpha\gamma}^{(1)}. \tag{63}$$

From Eq. (22), we obtain the first-order contracted pressure tensor

$$P_{\alpha\beta}^{(1)} = P_{\alpha\beta}^{*(1)}\left(1-\frac{\omega_2}{\omega_1}\right) - \frac{1}{\omega_1}\left(\partial_t^{(1)} P_{\alpha\beta}^{\rm eq} + \partial_\gamma Q_{\alpha\beta\gamma}^{\rm eq}\right), \tag{64}$$

which is used to find an expression for the first-order quasiequilibrium pressure tensor $P_{\alpha\beta}^{*(1)}$ using condition Eq. (62):

$$P_{\alpha\beta}^{*(1)} = -\frac{1}{\omega_2}\left(\partial_t^{(1)} P_{\alpha\beta}^{\rm eq} + \partial_\gamma Q_{\alpha\beta\gamma}^{\rm eq}\right). \tag{65}$$

Inserting Eq. (65) in Eq. (44), we obtain the expression for the second-order momentum equation:

$$\partial_t^{(2)} u_\alpha = -\frac{1}{\rho}\partial_\beta \Pi_{\alpha\beta} \tag{66}$$

where $\Pi_{\alpha\beta}$ is the nonequilibrium pressure tensor,

$$\Pi_{\alpha\beta} = -\mu\left(S_{\alpha\beta} - \frac{2}{D}\partial_\gamma u_\gamma \delta_{\alpha\beta}\right), \tag{67}$$

with

$$S_{\alpha\beta} = \partial_\alpha u_\beta + \partial_\beta u_\alpha, \tag{68}$$

the strain rate tensor, and

$$\mu = \left(\frac{1}{\omega_2} - \frac{1}{2}\right)\rho T. \tag{69}$$

Using condition Eq. (63), second-order energy equation is derived similarly for $\mathrm{Pr} < \mathrm{Pr_{BGK}}$ and is written as

$$\partial_t^{(2)} T = \frac{2}{\rho D}\partial_\alpha(\kappa\partial_\alpha T) - \frac{2}{\rho D}(\partial_\alpha u_\beta)\Pi_{\alpha\beta}, \tag{70}$$

where κ is the thermal conductivity given by

$$\kappa = \frac{D+2}{2}\left(\frac{1}{\omega_1} - \frac{1}{2}\right)\rho T. \tag{71}$$

With this last condition on the thermal conductivity for $\mathrm{Pr} > \mathrm{Pr_{BGK}}$, the thermo-hydrodynamic equations are derived over the entire range of Prandtl numbers.

3. *Thermohydrodynamic equations*

Summing up contributions of first and second order, the Fourier-Navier-Stokes equations are recovered as follows:

$$\partial_t \rho + \partial_\alpha(\rho u_\alpha) = 0, \tag{72}$$

$$\partial_t u_\alpha + u_\beta\partial_\beta u_\alpha = -\frac{1}{\rho}\partial_\alpha(\rho T) - \frac{1}{\rho}\partial_\beta \Pi_{\alpha\beta}, \tag{73}$$

$$\partial_t T = -u_\alpha \partial_\alpha T - \frac{2}{D} T(\partial_\alpha u_\alpha) - \frac{2}{\rho D}(\partial_\alpha u_\beta)\Pi_{\alpha\beta} + \frac{2}{\rho D}\partial_\alpha(\kappa \partial_\alpha T), \tag{74}$$

where, as before, the stress tensor is defined as

$$\Pi_{\alpha\beta} = -\mu\left(S_{\alpha\beta} - \frac{2}{D}\partial_\gamma u_\gamma \delta_{\alpha\beta}\right), \tag{75}$$

with the strain rate tensor,

$$S_{\alpha\beta} = \partial_\alpha u_\beta + \partial_\beta u_\alpha. \tag{76}$$

Expressions for viscosity and thermal conductivity as a function of the Prandtl number are given by

$$\mu(\mathrm{Pr}) = \begin{cases} \left(\frac{1}{\omega_1} - \frac{1}{2}\right)\rho T, & \text{if } \mathrm{Pr} \leqslant 1, \\ \left(\frac{1}{\omega_2} - \frac{1}{2}\right)\rho T, & \text{if } \mathrm{Pr} > 1, \end{cases} \tag{77}$$

and

$$\kappa(\mathrm{Pr}) = \begin{cases} \left(\frac{1}{\omega_2} - \frac{1}{2}\right)\rho T, & \text{if } \mathrm{Pr} \leqslant 1, \\ \left(\frac{1}{\omega_1} - \frac{1}{2}\right)\rho T, & \text{if } \mathrm{Pr} > 1. \end{cases} \tag{78}$$

$$F_i = W_i\left\{\rho + \frac{M_\alpha c_{i\alpha}}{T} + \frac{(M_{\alpha\beta} - \rho T\delta_{\alpha\beta})(c_{i\alpha}c_{i\beta} - T\delta_{\alpha\beta})}{2T^2} + \frac{[M_{\alpha\beta\gamma} - \rho T(u_\alpha\delta_{\beta\gamma} + u_\beta\delta_{\alpha\gamma} + u_\gamma\delta_{\alpha\beta})](c_{i\alpha}c_{i\beta}c_{i\gamma} - 3Tc_{i\gamma}\delta_{\alpha\beta})}{6T^3}\right\}, \tag{80}$$

where the weights $W_i(T)$ are computed according to Eq. (2), and the velocity set is composed of the following six energy shells:

$$C_0 = \{(0,0)\}, \quad C_1 = \{(0,\pm 1),(\pm 1,0)\},$$
$$C_2 = \{(\pm 1,\pm 1)\}, \quad C_3 = \{(0,\pm 3),(\pm 3,0)\},$$
$$C_4 = \{(\pm 1,\pm 3),(\pm 3,\pm 1)\}, \quad C_5 = \{(\pm 3,\pm 3)\},$$

a total of 25 velocities.

For equilibrium populations, the moments correspond to the momentum, pressure tensor, and energy flux tensor, respectively:

$$M_\alpha = \rho u_\alpha, \quad M_{\alpha\beta} = P^{\mathrm{eq}}_{\alpha\beta} = \rho T\delta_{\alpha\beta} + \rho u_\alpha u_\beta,$$
$$M_{\alpha\beta\gamma} = Q^{\mathrm{eq}}_{\alpha\beta\gamma} = \rho T\left(u_\alpha\delta_{\beta\gamma} + u_\beta\delta_{\alpha\gamma} + u_\gamma\delta_{\alpha\beta}\right) + \rho u_\alpha u_\beta u_\gamma. \tag{81}$$

For quasiequilibrium populations the second- and third-order moments are defined based on the Prandtl number. For $\mathrm{Pr} \leqslant \mathrm{Pr}_{\mathrm{BGK}}$:

$$M_{\alpha\beta} = P^*_{\alpha\beta} = P^{\mathrm{eq}}_{\alpha\beta}, \tag{82}$$

$$M_{\alpha\beta\gamma} = Q^*_{\alpha\beta\gamma} = Q_{\alpha\beta\gamma} - u_\alpha\left(P_{\beta\gamma} - P^{\mathrm{eq}}_{\beta\gamma}\right) - u_\beta\left(P_{\alpha\gamma} - P^{\mathrm{eq}}_{\alpha\gamma}\right) - u_\gamma\left(P_{\alpha\beta} - P^{\mathrm{eq}}_{\alpha\beta}\right). \tag{83}$$

For $\mathrm{Pr} > \mathrm{Pr}_{\mathrm{BGK}}$, we have

$$M_{\alpha\beta} = P^*_{\alpha\beta} = P_{\alpha\beta}, \tag{84}$$

$$M_{\alpha\beta\gamma} = Q^*_{\alpha\beta\gamma} = Q^{\mathrm{eq}}_{\alpha\beta\gamma} + u_\alpha\left(P_{\beta\gamma} - P^{\mathrm{eq}}_{\beta\gamma}\right) + u_\beta\left(P_{\alpha\gamma} - P^{\mathrm{eq}}_{\alpha\gamma}\right) + u_\gamma\left(P_{\alpha\beta} - P^{\mathrm{eq}}_{\alpha\beta}\right), \tag{85}$$

Finally, the expression for the Prandtl number becomes

$$\mathrm{Pr} = \begin{cases} \frac{(2-\omega_1)\omega_2}{(2-\omega_2)\omega_1}, & \text{if } \mathrm{Pr} \leqslant 1, \\ \frac{(2-\omega_2)\omega_1}{(2-\omega_1)\omega_2}, & \text{if } \mathrm{Pr} > 1. \end{cases}$$

E. Realization of the multispeed thermal lattice Boltzmann model

We now summarize the equations and expressions needed for the implementation of the higher-order thermal LB model. The lattice Boltzmann equation including quasiequilibrium model reads

$$f_i(\boldsymbol{x} + \boldsymbol{c}_i\delta t, t + \delta t) - f_i(\boldsymbol{x},t) = \omega_1(f_i^* - f_i) + \omega_2\left(f_i^{\mathrm{eq}} - f_i^*\right), \tag{79}$$

where the equilibrium and quasiequilibrium populations can be written in the compact form, until third order in velocity, as

where the second- and third-order tensors can be computed directly from populations:

$$P_{\alpha\beta} = \sum_{i=1}^{Q} f_i c_{i\alpha}c_{i\beta}, \tag{86}$$

$$Q_{\alpha\beta\gamma} = \sum_{i=1}^{Q} f_i c_{i\alpha}c_{i\beta}c_{i\gamma}. \tag{87}$$

The relaxation parameters ω_1 and ω_2 are computed by the corresponding viscosity and thermal conductivity:

$$\mu = \begin{cases} \left(\frac{1}{\omega_1} - \frac{1}{2}\right)\rho T, & \text{if } \mathrm{Pr} \leqslant 1, \\ \left(\frac{1}{\omega_2} - \frac{1}{2}\right)\rho T, & \text{if } \mathrm{Pr} > 1, \end{cases}$$

and

$$\kappa = \begin{cases} \left(\frac{1}{\omega_2} - \frac{1}{2}\right)\rho T, & \text{if } \mathrm{Pr} \leqslant 1, \\ \left(\frac{1}{\omega_1} - \frac{1}{2}\right)\rho T, & \text{if } \mathrm{Pr} > 1. \end{cases}$$

Finally, the thermal lattice Boltzmann algorithm is summarized in three main steps:

(1) Propagation step: populations associated to velocity $\boldsymbol{c}_i$ are displaced to the corresponding adjacent links:

$$f_i(\boldsymbol{x},t) \rightarrow f_i(\boldsymbol{x} + \boldsymbol{c}_i, t+1), \tag{88}$$

which results in a new set of populations, $f_i'(\boldsymbol{x},t)$.

(2) Wall boundary conditions: in the presence of walls, the missing populations at the wall are replaced according to the description given in Sec. II F.

(3) Collision step: in this last step, populations $f_i'(\boldsymbol{x},t)$ are over-relaxed by the rule

$$f_i'(\boldsymbol{x},t) \leftarrow f_i'(\boldsymbol{x},t) + \omega_1(f_i^* - f_i') + \omega_2\left(f_i^{\mathrm{eq}} - f_i^*\right), \tag{89}$$

where the two relaxation parameters, equilibrium populations and quasiequilibrium populations, have been previously described.

F. Improved TMS wall boundary conditions

Until now, the new thermal model presents features very similar to the standard lattice Boltzmann for isothermal flows; major changes are found only in the derivation of the proper weights corresponding to the ZOT lattice in case of energy conservation, and in the derivation of the equilibrium populations through entropic construction, pertinent to the changes in the lattice velocity set. However, one faces difficulties in the implementation of wall boundary conditions, since some of the populations are unknown and have to be reconstructed in an ad-hoc manner; furthermore, the treatment of the boundary conditions becomes even more complicated in the case of multispeed models because not only some populations lying on the wall are missing, but also populations associated to nodes residing in the "fluid" are missing. This is indicated in Fig. 1 for a flat wall, and where the "unknown populations" are shown in dashed lines. Two main approaches are popular in the literature for multispeed models: the kinetic-diffuse boundary conditions [35,36] or the so-called "regularized boundary conditions" [31,37]. In this work, an extension of the Tamm-Mott-Smith (TMS) boundary conditions presented in Ref. [10] including population treatment similar to Refs. [31,37] is described.

In the following, the main steps used to implement the boundary conditions are presented, making a clear difference in the case of nodes belonging to the wall and nodes belonging to the "fluid."

1. Wall-nodes boundaries

The first step in the wall-nodes boundary implementation is to replace the missing populations using the bounce-back scheme,

$$f_i^{\mathrm{bb}} = f_{-i}, \tag{90}$$

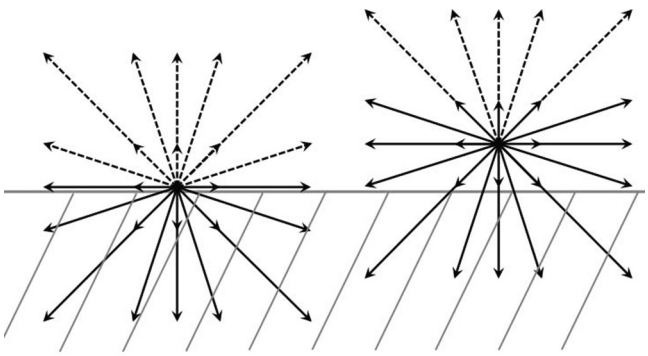

FIG. 1. Two boundary nodes for the D2Q25 lattice. Dashed arrows represent unknown populations.

thus guaranteeing no mass flux through the wall, and also allows us to find the target density at the wall, which can be computed as

$$\rho_{\mathrm{tgt}} = \sum_{i\in\overline{D}} f_i^{\mathrm{bb}} + \sum_{i\notin\overline{D}} f_i, \tag{91}$$

where $\overline{D}$ is the ensemble of the missing populations. Assuming that velocity and temperature at the wall are prescribed (Dirichlet boundary conditions), we can fix target velocity, density, and temperature to construct proper populations, which can substitute the missing ones. In the spirit of the TMS scheme, the precollision values of the populations belonging to the walls become

$$f_i \leftarrow f_i + f_i'(\rho_{\mathrm{tgt}},\boldsymbol{u}_{\mathrm{tgt}},T_{\mathrm{tgt}}) - f_i'(\rho_{\mathrm{loc}},\boldsymbol{u}_{\mathrm{loc}},T_{\mathrm{tgt}}). \tag{92}$$

It must be noted that in the TMS boundary condition, the populations f_i' are assumed to be of the form f_i^{eq}. We now modify this in the spirit regularized boundary conditions; populations f_i' are approximated by the equilibrium populations plus a contribution of the nonequilibrium part estimated as

$$f_i' \simeq f_i^{\mathrm{eq}}(\rho_{\mathrm{tgt}},\boldsymbol{u}_{\mathrm{tgt}},T_{\mathrm{tgt}}) + f_i^{(1)}(\rho_{\mathrm{tgt}},\boldsymbol{u}_{\mathrm{tgt}},T_{\mathrm{tgt}},\nabla u,\nabla T). \tag{93}$$

The equilibrium part of the previous expression is computed according to Eq. (5), while the nonequilibrium part is computed, as suggested in Ref. [37],

$$f_i^{(1)} = \frac{1}{2T^2} T_{i,\alpha\beta} P_{\alpha\beta}^{(1)} + \frac{1}{6T^3} I_{i,\alpha\beta\gamma} Q_{\alpha\beta\gamma}^{(1)}, \tag{94}$$

where

$$T_{i,\alpha\beta} = c_{i\alpha}c_{i\beta} - T\delta_{\alpha\beta}, \tag{95}$$

$$I_{i,\alpha\beta\gamma} = c_{i\alpha}c_{i\beta}c_{i\gamma} - T(c_{i\gamma}\delta_{\alpha\beta} + c_{i\beta}\delta_{\alpha\gamma} + c_{i\alpha}\delta_{\beta\gamma}), \tag{96}$$

and where $P_{\alpha\beta}^{(1)}$ and $Q_{\alpha\beta\gamma}^{(1)}$ are the first-order pressure tensor and heat flux tensor, respectively. Explicit formulation of the first-order pressure and heat flux tensors is obtained by Chapman-Enskog analysis and lead to

$$P_{\alpha\beta}^{(1)} = -\frac{1}{\omega}\rho T\left(S_{\alpha\beta} - \frac{2}{D}\partial_\gamma u_\gamma \delta_{\alpha\beta}\right), \tag{97}$$

$$Q_{\alpha\beta\gamma}^{(1)} = -\frac{1}{\omega}\rho T[\partial_\alpha T\delta_{\beta\gamma} + \partial_\beta T\delta_{\alpha\gamma} + \partial_\gamma T\delta_{\alpha\beta}] + u_\alpha P_{\beta\gamma}^{(1)} + u_\beta P_{\alpha\gamma}^{(1)} + u_\gamma P_{\alpha\beta}^{(1)}, \tag{98}$$

where ω depends on the value of the Pr number. Deviating from what was reported in Ref. [37], first-order pressure tensor and heat flux tensor are computed by directly applying Eqs. (97) and (98) by computation of derivatives of velocity and temperature with a second-order accurate finite-difference scheme, similar to Ref. [38]. As is the case in Ref. [37], all the populations are replaced by the new ones computed by the procedure reported before, in order to obtain the correct target values at the wall nodes. It must be noted that the TMS boundary condition by construction does not allow slip phenomenon for microflows since the target macroscopic values are chosen for a no-slip wall. Other boundary conditions, such as the diffuse reflection boundary conditions [35], are more suited for microflow applications.

2. *Fluid-nodes boundaries*

As discussed above, to complete the boundary implementation, also precollision values of missing populations belonging to the fluid nodes need to be computed. For this type of nodes the target density, velocity, and temperature are chosen to be the local quantities of the previous time step, while velocity and temperature gradients are computed as reported for the nodes belonging to the wall. Given target quantities, the TMS algorithm can be applied, as for the nodes belonging to the wall. Another slight difference with the procedure reported in Ref. [37], however, is that at the fluid-boundary nodes only the missing populations are substituted; this guarantees that a minimal amount of information is lost during the boundary implementation.

G. Entropic thermal lattice Boltzmann formulation

To conclude the theoretical part of this work, extension of the higher-order TLBM to the entropic thermal lattice Boltzmann method (ETLBM) is presented in the following, based on the entropic LBM of Ref. [8]. Such an extension allows us to enhance stability of subgrid simulations. In this case, Eq. (9) is replaced by the following two equations, which depends on the Prandtl number. If $\mathrm{Pr} < \mathrm{Pr}_{\mathrm{BGK}}$,

$$f_i(\boldsymbol{x}+\boldsymbol{c}_i\delta t, t+\delta t) - f_i(\boldsymbol{x},t) = \alpha\beta\left(f_i^* - f_i\right) + \omega_2\left(f_i^{\mathrm{eq}} - f_i^*\right), \tag{99}$$

while if $\mathrm{Pr} > \mathrm{Pr}_{\mathrm{BGK}}$,

$$f_i(\boldsymbol{x}+\boldsymbol{c}_i\delta t, t+\delta t) - f_i(\boldsymbol{x},t) = \omega_1\left(f_i^* - f_i\right) + \alpha\beta\left(f_i^{\mathrm{eq}} - f_i^*\right). \tag{100}$$

In the above equations, equilibrium populations f_i^{eq} are the same as in Eq. (9) and correspond to the minimizer of the entropy function Eq. (1), pertinent with the entropic construction, while the relaxation parameter related to the viscosity is replaced by $\alpha\beta$, where α is the maximal over-relaxation parameter, which is the positive root of the entropy condition:

$$H[f + \alpha(f^{\mathrm{eq}} - f)] = H(f). \tag{101}$$

Viscosity is now parametrized by β_1 or β_2 for Prandtl number lower or higher than $\mathrm{Pr}_{\mathrm{BGK}}$, respectively:

$$\mu(\mathrm{Pr}) = \begin{cases} \frac{1}{2}\left(\frac{1}{\beta_1} - 1\right)\rho T, & \text{if } \mathrm{Pr} \leqslant \mathrm{Pr}_{\mathrm{BGK}}, \\ \frac{1}{2}\left(\frac{1}{\beta_2} - 1\right)\rho T, & \text{if } \mathrm{Pr} > \mathrm{Pr}_{\mathrm{BGK}}. \end{cases}$$

This formulation is based on the assumption that entropy estimate Eq. (101) serves to stabilize the flow only through viscosity, without affecting the thermal conductivity. This means that application of the ELBM in the context of thermal flows is to capture the subgrid dynamics of the velocity only. In the numerical validation part, both standard and entropic realizations are tested and validated.

III. NUMERICAL VALIDATION

To validate the above thermal lattice Boltzmann model for compressible flows at low Mach numbers, five different classical numerical setups were considered. The planar thermal Couette flow, and the Rayleigh-Bénard natural convection were simulated as standard benchmarks for thermal models. Moreover, the effect of increasing Mach number was tested by means of propagation of acoustic waves; and the independence of the sound speed from the reference lattice temperature has been shown. Finally, shock tube simulations have been performed as a further benchmark.

A. Thermal Couette flow

The thermal Couette flow problem is used to test the capability of the current model in evaluating the viscous heat dissipation for different Prandtl numbers. The bottom wall of the domain was kept at a temperature T_C and at rest, while the top wall had a temperature $T_H > T_C$ and a uniform wall velocity U. The analytical solution for the velocity field is a simple linear profile; while the solution for temperature can be written using reduced temperature, $(T - T_C)/(T_H - T_C)$, as

$$\frac{T - T_C}{T_H - T_C} = \frac{y}{H} + \frac{\mathrm{Pr}\cdot\mathrm{Ec}}{2}\frac{y}{H}\left(1 - \frac{y}{H}\right), \tag{102}$$

where y is the perpendicular distance from the bottom wall, H is the height of the channel, $\mathrm{Pr} = c_p\mu/\kappa$ is the Prandtl number, and $\mathrm{Ec} = U^2/[c_p\,(T_H - T_C)]$ is the Eckert number with $c_p = 2$. These simulations were performed in a wide range of Pr and Ec numbers, with the following parameters: $U = 0.05$, $H = 100$, $T_C = 0.3675$, $\mu = 0.025$; other parameters can be defined using the Prandtl and Eckert numbers. Periodic boundary conditions were applied in the horizontal direction, while at the bottom and top walls, the wall boundary condition described in Sec. II F was applied. Figure 2 represents the results of the simulation for different Eckert numbers; the Prandtl number is fixed to $\mathrm{Pr} = 0.71$.

The results, for fixed Eckert number $\mathrm{Ec} = 8.0$ and variable Prandtl numbers, are shown in Fig. 3. Both Figs. 2 and 3 demonstrate that the present thermal lattice Boltzmann model recovers the analytical solution with a good accuracy.

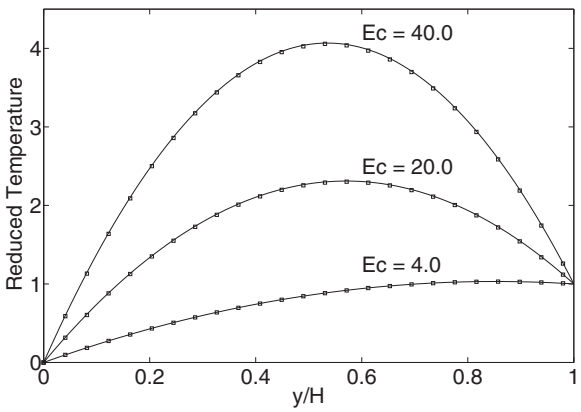

FIG. 2. Temperature profile of the thermal Couette flow at various Eckert numbers for the fixed Prandtl number $\mathrm{Pr} = 0.71$. The solid lines represent the analytical solutions, while the symbols represent the simulations.

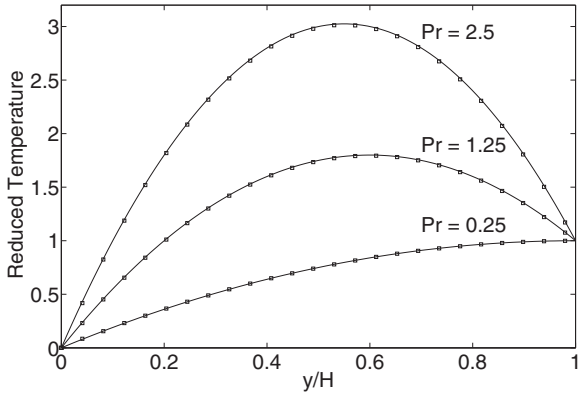

FIG. 3. Temperature profile of the thermal Couette flow at various Prandtl numbers for the fixed Eckert number Ec = 8.0. The solid lines represent the analytical solutions, while the symbols represent the simulations.

B. Shock tube: The sod's problem

For a further validation, the classical shock tube problem was studied. The quasi-one-dimensional setup consists of a tube, with two separated domains characterized by different temperatures, densities, and pressures. The left and the right side of the domain can be imagined to be separated by a membrane in the center of the tube and as soon as the membrane is removed, a discontinuity is formed, thus resulting in a compression wave traveling into the lower-pressure region and a rarefaction wave traveling into the high-pressure region. Results are shown in Fig. 4 for the following parameters: $T_L = 0.4375$, $\rho_L = 1.2$, $P_L = 0.525$ for the left side, and $T_R = 0.35$, $\rho_R = 1.0$, $P_R = 0.35$ for the right side. The viscosity was set to $\mu = 0.01$ and the simulation was run with standard BGK and with entropic estimate Eq. (101). The result shows how entropy estimate can damp some oscillations near the shock front.

C. Rayleigh-Bénard natural convection

The Rayleigh-Bénard natural convection is an other classical setup that is often used to validate thermal lattice

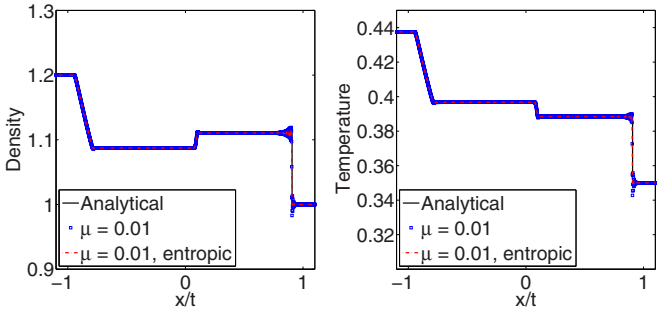

FIG. 4. (Color online) Shock tube simulation for the values $T_L = 0.4375$, $\rho_L = 1.2$, $P_L = 0.525$ for the left side, and $T_R = 0.35$, $\rho_R = 1.0$, $P_R = 0.35$ for the right side. The black solid line represents the analytical solution; circular blue markers show the simulation with a viscosity of $\mu = 0.01$; square red markers show the simulation with the employment of entropic estimate.

Boltzmann models. In this setup, a viscous fluid is heated by a bottom wall at temperature T_H and cooled by a top wall at temperature T_C. This setup is characterized by the Rayleigh number defined as Ra = GrPr, where Gr is the Grashof number $\mathrm{Gr} = g\beta\,(T_H - T_C)\,H^3/\nu^2$, g is the acceleration due to gravity, $\beta = 1/T$ is the thermal expansion coefficient, and H is the distance between the walls. For a Rayleigh number lower than a critical value, Ra_c, a static solution exists, where a linear temperature gradient is observed between hot and cold walls; and the heat transfer is dictated only by thermal conduction. As soon as the critical Rayleigh number, Ra_c, becomes larger than the critical value, the linear temperature gradient becomes unstable and the system starts to convect. Implementation of the gravitational force is done by following the exact difference method of Ref. [39]; and the kinetic Eq. (9) is replaced by

$$\begin{aligned} f_i(\boldsymbol{x} + \boldsymbol{c}_i\delta t, t + \delta t) - f_i(\boldsymbol{x}, t) \\ = \omega_1(f_i^* - f_i) + \omega_2\left(f_i^{\mathrm{eq}}(\boldsymbol{u}) - f_i^*\right) \\ + \left[f_i^{\mathrm{eq}}(\boldsymbol{u} + \Delta\boldsymbol{u}) - f_i^{\mathrm{eq}}(\boldsymbol{u})\right]. \end{aligned} \tag{103}$$

The last term on the right-hand side of Eq. (103) takes into account the change in velocity due to the presence of the acceleration $\boldsymbol{a}$ per time step $\delta t = 1$, $\Delta\boldsymbol{u} = \boldsymbol{a}\delta t$. Since the force due to gravity can be written as $\boldsymbol{F} = \boldsymbol{g}\,(\rho - \rho_\infty)$, the change of velocity becomes $\Delta\boldsymbol{u} = \frac{1}{\rho}\boldsymbol{g}\,(\rho - \rho_\infty)$, where ρ_∞ is the reference density used for initializing the setup. The simulations were initialized with a temperature gradient,

$$T(x, y) = T_H - \Delta T\,\frac{y}{H}, \tag{104}$$

superimposed with a disturbance,

$$T'(x, y) = 0.01\Delta T \sin\left(\frac{\pi x}{L}\right)\sin\left(\frac{\pi y}{H}\right), \tag{105}$$

and zero flow velocity. To initialize the density the simulation was run for 50 000 time steps by keeping temperature and velocity in the equilibrium fixed to the initialization values. In Fig. 5, temperature distributions for the simulation run at Ra = 2 000, Ra = 10 000, and Ra = 50 000 are shown. Above the critical value for the Rayleigh number, the heat transfer at the cold and hot walls is increased due to convection. The Nusselt number, Nu, describes the heat transfer,

$$\mathrm{Nu} = -\frac{H}{L\Delta T}\sum_{k=1}^{L}\frac{\partial T(k)}{\partial y}, \tag{106}$$

where the temperature derivative was computed by a second-order finite differences method. The mean Nusselt number between cold and hot walls computed by the simulations is compared with the reference results of Ref. [40] in Fig. 6 for a grid size of 200 × 100. One can see that the simulation recovers accurately the reference values of Ref. [41].

Moreover, the Ra_c, above which convection starts, is computed by measuring the mean growth rate of velocity r in the middle of the domain,

$$r = \frac{v_m(t) - v_m(t-1)}{v_m(t)}, \tag{107}$$

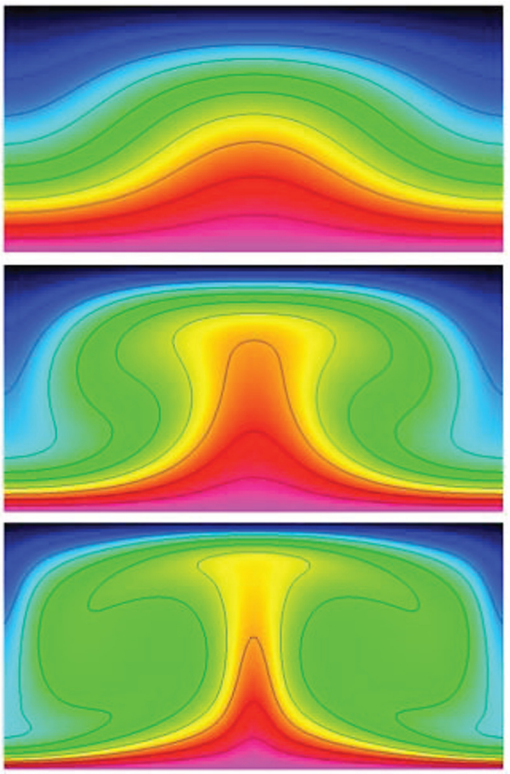

FIG. 5. (Color online) Temperature distribution at Ra = 2 000, Ra = 10 000 and Ra = 50 000. A total of 10 uniformly spaced temperature contours are displayed.

with the mean vertical velocity

$$v_m(t) = \sum_{j=0}^{H} u(L/2, j, t), \tag{108}$$

for Rayleigh numbers slightly above the critical value. Ra_c was obtained by extrapolation of the measurements to the zero growth rate, and is $\mathrm{Ra}_c = 1717.5$; with a relative error with respect to the theoretical value of $\epsilon = 0.6\%$ [16], on a grid size of 600×300.

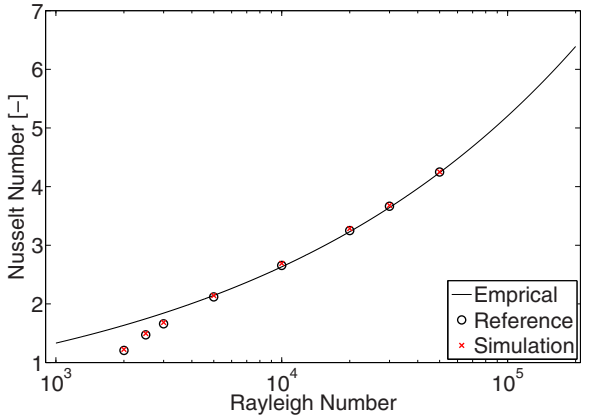

FIG. 6. (Color online) Nusselt number comparison with reference values [40] and empirical correlation $\mathrm{Nu} = 1.56(\mathrm{Ra}/\mathrm{Ra_c})^{0.296}$, for different Rayleigh number values.

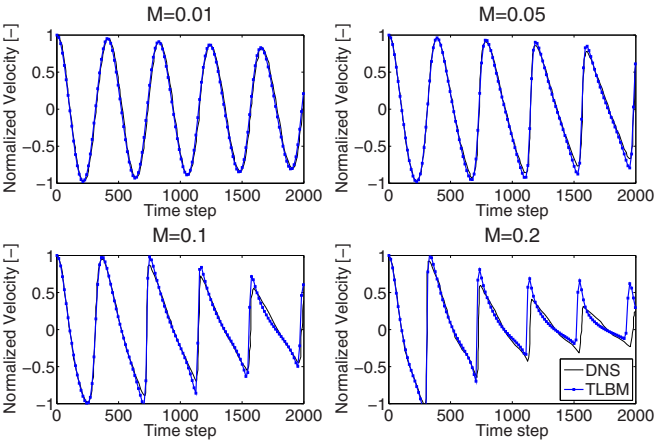

FIG. 7. (Color online) Velocity evolution of the sound wave measured at $N_x/4$ for different initial amplitudes proportional to the Mach number.

D. Plane sound wave

The performance of the present thermal lattice Boltzmann model was also tested for linear and nonlinear acoustic cases, by means of simulation of acoustic waves with various amplitudes. Initial conditions are given as

$$u_x(x,y) = \mathrm{Ma}\, c_s \sin\left(\frac{2\pi x}{L}\right), \tag{109}$$

$$u_y(x,y) = 0, \tag{110}$$

$$\rho(x,y) = \rho_0\left[1.0 + \mathrm{Ma}\sin\left(\frac{2\pi x}{L}\right)\right], \tag{111}$$

where Ma is Mach number varied in the range [0.01,0.2], $L = 256$ is the length of the domain, $c_s = \sqrt{2T}$ the speed of sound, and the viscosity is set to $\mu = 0.025$. Periodic boundary conditions were used in the x and y direction. The simulations results of the present model are compared with spectral element method of Ref. [42] in Fig. 7 and shows how the present model is able to recover nonlinear effects

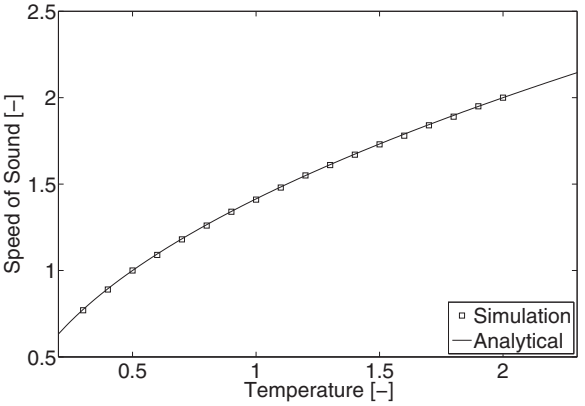

FIG. 8. Sound speed as a function of the temperature. Squares, simulation results; solid line, theoretical value $c_s = \sqrt{2T}$.

(so called "N-shaped" waves) that appear with increasing Mach numbers.

E. Reference temperature independence

Further validation of the model is performed by measuring the speed of sound for different temperatures. The measurements are carried out by introducing a pressure difference $\Delta p = 10^{-3}$ in a quasi-2D setup, and by measuring the time required by the shock front to reach a determined distance. The results are reported in Fig. 8 and show how the present higher-order thermal model is able to reproduce the correct speed of sound irrespective the lattice reference temperature.

IV. CONCLUSIONS

We have presented a novel thermal model-based entropic theory of admissible higher-order lattices. This model is capable of correctly reproducing viscous heating, heat conduction, and linear and nonlinear acoustic effects. In particular, the model is free of any correction terms and uses only one set of population to correctly reproduce the moment system necessary to derive the Fourier-Navier-Stokes equations, thus maintaining the simplicity of an isothermal lattice Boltzmann model.

To ensure practical usability of the model, wall boundary conditions capable of handling arbitrary geometries was also described in detail. Moreover, with extensions such as the entropic formulation for subgrid simulations, the model is nonlinearly stable and enables simulations of fluid turbulence. The numerical validation through five classical setups have shown excellent performance for a wide range of applications.

ACKNOWLEDGMENTS

This work was supported by European Research Council (ERC) Advanced Grant No. 291094-ELBM. Computational resources from the Swiss National Super Computing Center CSCS were provided under the Grant No. s492.

APPENDIX: EQUILIBRIUM LAGRANGE MULTIPLIERS

$$\chi = 1 - \frac{u^2}{2T} + \frac{(3-T)(3T-1)\left(u_x^4+u_y^4\right)+4T^2u_x^2u_y^2}{16T^4} + \chi^{(6)} + \chi^{(8)}$$

$$\chi^{(6)} = \frac{u^2\left(\{81+T[T(982-516T+69T^2)-516]\}\left(u_x^4+u_y^4\right)\right)}{384T^7} + \frac{4T\{T[3T(5T-12)+29]-6\}u_x^2u_y^2}{384T^7}$$

$$\begin{aligned}\chi^{(8)} = {} & \frac{\{T[T(T\{T[(10\,058-639T)T-43\,683]+73\,876\}-51\,321)+15\,498]-1\,701\}\left(u_x^8+u_y^8\right)}{6144T^{10}} \\ & - \frac{4\{T[T(T\{T[T(1\,545T-11\,566)+33\,155]-43\,788\}+26\,307)-7182]+729\}\left(u_x^6u_y^2+u_x^2u_y^6\right)}{6144T^{10}} \\ & - \frac{6\{567+T[-5310+T(18\,291+T\{-27\,980+T[18\,329+T(-4830+349T)]\})]\}u_x^4u_y^4}{6144T^{10}}\end{aligned}$$

$$\begin{aligned}\zeta_x = {} & 1+\frac{u_x}{T}+\frac{u_x^2}{2T^2}+\frac{u_x^3}{6T^3}+\frac{u_x^4}{24T^4}+\frac{[-5-9(T-2)T]u_x^5-3[3+5(T-2)T]u_xu_y^4}{48T^5}+\frac{[16-27(T-2)T]u_x^6-9[5(T-2)T+3]u_x^2u_y^4}{144T^6} \\ & + \frac{[4T-3T^2(15T^2-84T+106)-81]u_x^7-27(5T^2-2T+3)^2u_x^5u_y^2-9(5T^2-10T+3)(5T^2-6T+3)u_x^3u_y^4-3\{T[T(141T^2-676T+1\,030)-516]+81\}u_xu_y^6}{1152T^8} \\ & + \frac{[467T-3T^2(15T^2-128T+266)-81]u_x^8-27(5T^2-10T+3)^2u_x^6u_y^2-3(5T^2-10T+3)(15T^2-26T+9)u_x^4u_y^4-3\{T[T(141T^2-676T+1\,030)-516]+81\}u_x^2u_y^6}{1152T^9}\end{aligned}$$

$$\begin{aligned}\zeta_y = {} & 1+\frac{u_y}{T}+\frac{u_y^2}{2T^2}+\frac{u_y^3}{6T^3}+\frac{u_y^4}{24T^4}+\frac{[-5-9(T-2)T]u_y^5-3[3+5(T-2)T]u_yu_x^4}{48T^5}+\frac{[16-27(T-2)T]u_y^6-9[5(T-2)T+3]u_y^2u_x^4}{144T^6} \\ & + \frac{[4T-3T^2(15T^2-84T+106)-81]u_y^7-27(5T^2-2T+3)^2u_y^5u_x^2-9(5T^2-10T+3)(5T^2-6T+3)u_y^3u_x^4-3\{T[T(141T^2-676T+1030)-516]+81\}u_yu_x^6}{1152T^8} \\ & + \frac{[467T-3T^2(15T^2-128T+266)-81]u_y^8-27(5T^2-10T+3)^2u_y^6u_x^2-3(5T^2-10T+3)(15T^2-26T+9)u_y^4u_x^4-3\{T[T(141T^2-676T+1\,030)-516]+81\}u_y^2u_x^6}{1152T^9}\end{aligned}$$

$$\begin{aligned}\gamma = {} & 1+\frac{(5T^2-10T+3)\left(u_x^4+u_y^4\right)}{32T^5}+\frac{\{T[T(141T^2-676T+1030)-516]+81\}\left(u_x^6+u_y^6\right)+9(5T^2-10T+3)^2\left(u_x^4u_y^2+u_x^2u_y^4\right)}{768T^8} \\ & + \frac{[1701+T(-15\,444+T\{51\,609+T[-77\,128+3T(16\,841-4540T+349T^2)]\})]\left(u_x^8+u_y^8\right)}{12\,288T^{11}} \\ & \times \frac{+(36+60T^2-120T)\{81+T[-528+T(1100-788T+183T^2)]\}(vx^6vy^2+\mathrm{vx}^2\mathrm{vy}^6)}{12\,288T^{11}} \\ & + \frac{6(5T^2-10T+3)(T\{T[5T(29T-210)+2034]-1134\}+189)u_x^4u_y^4}{12\,288T^{11}}\end{aligned}$$

[1] H. Chen, S. Kandasamy, S. Orszag, R. Shock, S. Succi, and V. Yakhot, Science **301**, 633 (2003).

[2] S. Succi, *The Lattice Boltzmann Equation: For Fluid Dynamics and Beyond* (Oxford University Press, Oxford, 2001).

[3] M. Mendoza, I. Karlin, S. Succi, and H. J. Herrmann, Phys. Rev. D **87**, 065027 (2013).

[4] R. Benzi, S. Succi, and M. Vergassola, Phys. Rep. **222**, 145 (1992).

[5] H. Chen, S. Chen, and W. H. Matthaeus, Phys. Rev. A **45**, R5339 (1992).

[6] Y. Qian, D. d'Humières, and P. Lallemand, Europhys. Lett. **17**, 479 (1992).

[7] S. Chen and G. D. Doolen, Ann. Rev. Fluid Mech. **30**, 329 (1998).

[8] I. Karlin, A. Ferrante, and H. Öttinger, Europhys. Lett. **47**, 182 (1999).

[9] I. V. Karlin, S. Succi, and S. S. Chikatamarla, Phys. Rev. E **84**, 068701 (2011).

[10] S. Chikatamarla and I. Karlin, Physica A: Stat. Mech. Appl. **392**, 1925 (2013).

[11] X.-L. Li, D.-X. Fu, Y.-W. Ma, and X. Liang, Acta Mech. Sinica **26**, 795 (2010).

[12] Y. H. Qian and S. A. Orszag, Europhys. Lett. **21**, 255 (1993).

[13] N. I. Prasianakis and I. V. Karlin, Phys. Rev. E **76**, 016702 (2007).

[14] X. He, S. Chen, and G. D. Doolen, J. Comput. Phys. **146**, 282 (1998).

[15] Z. Guo, C. Zheng, B. Shi, and T. S. Zhao, Phys. Rev. E **75**, 036704 (2007).

[16] I. V. Karlin, D. Sichau, and S. S. Chikatamarla, Phys. Rev. E **88**, 063310 (2013).

[17] F. J. Alexander, S. Chen, and J. D. Sterling, Phys. Rev. E **47**, R2249 (1993).

[18] G. McNamara, A. Garcia, and B. Alder, J. Stat. Phys. **81**, 395 (1995).

[19] S. S. Chikatamarla and I. V. Karlin, Phys. Rev. Lett. **97**, 190601 (2006).

[20] S. S. Chikatamarla and I. V. Karlin, Phys. Rev. E **79**, 046701 (2009).

[21] S. Chikatamarla, C. Frouzakis, I. Karlin, A. Tomboulides, and K. Boulouchos, J. Fluid Mech. **656**, 298 (2010).

[22] D. N. Siebert, L. A. Hegele, and P. C. Philippi, Phys. Rev. E **77**, 026707 (2008).

[23] X. Shan, X.-F. Yuan, and H. Chen, J. Fluid Mech. **550**, 413 (2006).

[24] P. C. Philippi, L. A. Hegele, Jr, L. O. E. dos Santos, and R. Surmas, Phys. Rev. E **73**, 056702 (2006).

[25] D. N. Siebert, L. A. Hegele, Jr, R. Surmas, L. O. E. Dos Santos, and P. C. Philippi, Int. J. Modern Phys. C **18**, 546 (2007).

[26] W. P. Yudistiawan, S. K. Kwak, D. V. Patil, and S. Ansumali, Phys. Rev. E. **82**, 046701 (2010).

[27] J. W. Shim and R. Gatignol, Phys. Rev. E **83**, 046710 (2011).

[28] G. Vahala, P. Pavlo, L. Vahala, and N. S. Martys, Int. J. Modern Phys. C **9**, 1247 (1998).

[29] B. Piaud, S. Blanco, R. Fournier, and M. J. Clifton, J. Stat. Phys. **121**, 119 (2005).

[30] S. Ansumali, S. Arcidiacono, S. S. Chikatamarla, N. I. Prasianakis, A. N. Gorban, and I. V. Karlin, Eur. Phys. J. B **56**, 135 (2007).

[31] J. Latt, B. Chopard, O. Malaspinas, M. Deville, and A. Michler, Phys. Rev. E **77**, 056703 (2008).

[32] X. Shan and X. He, Phys. Rev. Lett. **80**, 65 (1998).

[33] S. Ansumali, I. Karlin, and H. Öttinger, Europhys. Lett. **63**, 798 (2003).

[34] S. S. Chikatamarla, S. Ansumali, and I. V. Karlin, Phys. Rev. Lett. **97**, 010201 (2006).

[35] S. Ansumali and I. V. Karlin, Phys. Rev. E **66**, 026311 (2002).

[36] J. Meng and Y. Zhang, J. Comput. Phys. **258**, 601 (2014).

[37] O. Malaspinas, B. Chopard, and J. Latt, Comput. Fluids **49**, 29 (2011).

[38] P. A. Skordos, Phys. Rev. E **48**, 4823 (1993).

[39] A. L. Kupershtokh, in *Proceedings of the Fifth International EHD Workshop, August 30-31, 2004* (University of Poitiers, France, 2004), pp. 241–246.

[40] R. Clever and F. Busse, J. Fluid Mech. **65**, 625 (1974).

[41] X. Shan, Phys. Rev. E **55**, 2780 (1997).

[42] G. Házi and P. Kávrán, J. Phys. A: Math. Gen. **39**, 3127 (2006).